

CONF-9310164--7

LA-UR- 93-3528

**Title:** Prototype Explosives Detection System Based on Nuclear Resonance Absorption in Nitrogen

**Author(s):** R. E. Morgado, G. Arnone, C. C. Cappiello, S. D. Gardner, C. L. Hollas, L. E. Ussery, J. M. White, J. D. Zahrt, and R. A. Krauss

**Submitted to:** SPIE Conference  
October 5-8, 1993  
Innsbruck, AUSTRIA

**MASTER**

**DISTRIBUTION OF THIS DOCUMENT IS UNLIMITED**

**Los Alamos**  
NATIONAL LABORATORY

Los Alamos National Laboratory, an affirmative action/equal opportunity employer, is operated by the University of California for the U.S. Department of Energy under contract W-7405-ENG-36. By acceptance of this article, the publisher recognizes that the U.S. Government retains a nonexclusive, royalty-free license to publish or reproduce the published form of this contribution, or to allow others to do so, for U.S. Government purposes. The Los Alamos National Laboratory requests that the publisher identify this article as work performed under the auspices of the U.S. Department of Energy.

Form No. 836-110  
BT 7629 10/91



**Prototype explosives detection system  
based on nuclear resonance absorption in nitrogen**

**R. E. Morgado, G. Arnone, C. C. Cappiello, S. D. Gardner,  
C. L. Hollas, L. E. Ussery, J. M. White, J. D. Zahrt.**

**Los Alamos National Laboratory, Los Alamos, NM 87545**

**R. A. Krauss,**

**Federal Aviation Administration, Atlantic City International Airport, NJ 08405**

**ABSTRACT**

A prototype explosives detection system that was developed for experimental evaluation of a nuclear resonance absorption technique is described. The major subsystems are a proton accelerator and beam transport, high-temperature proton target, an airline-luggage tomographic inspection station, and an image-processing/detection-alarm subsystem. The detection system performance, based on a limited experimental test, is reported.

**1. INTRODUCTION AND BACKGROUND**

The development of the pre-prototype explosives detection system described here is based on an earlier feasibility study<sup>1</sup> completed in 1989 in which the detection of nitrogen in an explosive simulant was demonstrated by scanning it with a gamma-ray beam of an energy corresponding to a nuclear resonance in nitrogen<sup>2</sup>. Our earlier study also suggested that, by this technique, certain explosives should be distinguishable from inert materials commonly encountered in airline passenger luggage.

Scaling from these results, it was projected that a very high current ( $\approx 15$  mA) proton accelerator, used in generating the resonant energy gamma rays, would be needed to meet the Federal Aviation Administration's (FAA's) 6s/bag throughput requirement. The developmental efforts described here were originally scoped to include the development of this high-current accelerator for a fully operational, semi-automated prototype detection system for test and evaluation in an airport. However, due to budget constraints, the scope of the project was scaled back to that of a laboratory test of a reduced throughput, non-automated system. Thus, some of the major subsystems that have been developed incorporate some of the design features of an airport prototype, e.g., the detector, data acquisition, and image processing subsystems, while the accelerator and related subsystems are for a reduced throughput (by an order of magnitude). Nevertheless, this pre-prototype system permits evaluation of many of the important operational characteristics of an airport system, which is the principal objective of the project.

In the following, the physical basis of the detection concept will be presented, followed by a description of each major subsystem and its key performance characteristics, and some results of our initial explosives detection tests from which preliminary conclusions on overall system performance are drawn.

This FAA-sponsored project was a collaborative effort of the Los Alamos National Laboratory (LANL) and the Sandia Nuclear Research Center (SNRC). Two variants of the detector/luggage inspection system were pursued by the respective collaborators, but using a common accelerator/gamma-ray production system. The following addresses the LANL detection approach; the SNRC approach is addressed in a companion paper.

**DISCLAIMER**

This report was prepared as an account of work sponsored by an agency of the United States Government. Neither the United States Government nor any agency thereof, nor any of their employees, makes any warranty, express or implied, or assumes any legal liability or responsibility for the accuracy, completeness, or usefulness of any information, apparatus, product, or process disclosed, or represents that its use would not infringe privately owned rights. Reference herein to any specific commercial product, process, or service by trade name, trademark, manufacturer, or otherwise does not necessarily constitute or imply its endorsement, recommendation, or favoring by the United States Government or any agency thereof. The views and opinions of authors expressed herein do not necessarily state or reflect those of the United States Government or any agency thereof.

## 2. PHYSICAL BASIS OF THE DETECTION CONCEPT

The strong resonance photoproton cross section of nitrogen,  $^{14}\text{N}(\gamma, p)^{13}\text{C}$ , is described by the Breit-Wigner equation:

$$\sigma(E_\gamma) = \pi \lambda^2 g \Gamma_\gamma \Gamma_p / [(E_\gamma - E_R)^2 + (\Gamma/2)^2] \quad (1)$$

Where:

$$\begin{aligned} \lambda &= \hbar c / E_\gamma = 21.5 \text{ fm} & \Gamma_\gamma &= 7 \text{ eV} \\ E_R &= 9.17 \text{ MeV} & \Gamma_p &= 115 \text{ eV} \\ g &= 2J + 1/2(2I + 1) = 5/6 & \Gamma &= 122 \text{ eV} \end{aligned}$$

The cross section for nitrogen near the 9.17-MeV resonance<sup>3,4,5</sup> is shown in Figure 1.

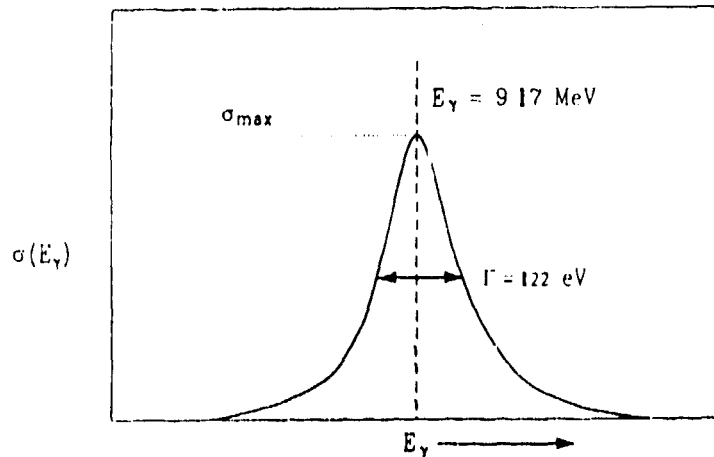


Figure 1.  $^{14}\text{N}$  nuclear resonance absorption cross section.

The extreme narrowness of this peak in the resonance, while representing a unique signature for nitrogen, presents a serious practical problem in generating an adequate resonant-energy gamma-ray flux for it to be a useful probe. After briefly investigating filtered bremsstrahlung sources, we found them to have adverse signal-to-noise ratios, and this led us to adopt the  $^{13}\text{C}(p, \gamma)^{14}\text{N}$  reaction<sup>6</sup> (the inverse to resonance absorption) as the preferred gamma-ray source. The proton source for this reaction dictates the use of a particle accelerator and the practicality of the approach depends largely on achieving sufficiently high proton currents from the accelerator.

Because of the Doppler shift from the recoiling  $^{14}\text{N}$  in the above reaction, only those gamma rays emitted in an  $\approx 0.7$ -degree-wide beam at  $80.7$  degrees from the direction of the proton beam (in the laboratory frame of reference) are at the precise resonance energy. Thus, the locus of resonant photons is a narrow  $80.7^\circ$  conical section whose axis coincides with the proton beam.

The transmission of a resonant energy beam through a volume containing both nitrogen and other material is given by:

$$T_R = I_R/I_0 = \exp[-(f\sigma_R + \sigma_{NR})\Delta m] \quad (2)$$

where the total cross section is the sum of resonance cross section,  $\sigma_R$ , and that for the nonresonant processes,  $\sigma_{NR}$ ;  $f$  is the mass fraction of nitrogen, and  $\Delta m$  the total mass thickness in atoms/cm<sup>2</sup>. The non-resonant attenuation,

$$T_{NR} = I_{NR}/I_0 = \exp(-\sigma_{NR}\Delta m), \quad (3)$$

can be determined independently from simultaneous off-resonance measurements of gamma-ray transmission. Thus, the nitrogen mass thickness is

$$\Delta N = f \Delta m = (1/\sigma_R) \ln (T_{NR} / T_R). \quad (4)$$

The off-resonance measurement is done by including barium fluoride in the  $^{13}\text{C}$  target, which produces 6.13-, 6.9-, and 7.1-MeV gamma rays from the  $(p,\alpha\gamma)$  reaction in  $^{19}\text{F}$ . Transmission measurements at these energies can be extrapolated to the resonant energy with sufficient accuracy to determine the nonresonant contribution to the total cross section. Transmission measurements through liquid nitrogen were used in determining the effective  $\sigma_R$  for the actual measurement system. A schematic of the detection concept is shown in Fig 2.

### 3. OVERALL DESCRIPTION OF THE PROTOTYPE DETECTION SYSTEM

Figure 3 shows the physical layout of the principal subsystems of the detection system. The accelerator produces a horizontal, pulsed beam of 1.75-MeV protons, which passes through a focusing quadrupole and beam energy debuncher, and is turned downward by a combination bending and focusing magnet to produce a ~1-cm-dia beam spot on the  $^{13}\text{C}$  target. The resultant conical fan beam of gamma rays is approximately (within  $10^\circ$ ) horizontal. Luggage is positioned onto the surface of a platform that incrementally rotates  $360^\circ$  to produce multiple views of a slice of the luggage. The luggage platform is raised or lowered by a constant increment (the "slice" thickness) between the successive rotational scans, until the vertical cross section of the bag has been scanned.

An array of gamma-ray detectors is positioned on the locus of the resonant energy beam, which spans approximately one quadrant of the fan beam. Individual detector outputs are collected, preprocessed, and transmitted to a computer work station and temporarily stored in the data acquisition work station. Upon completion of a luggage inspection, the data are transmitted to a second computer work station for a tomographic reconstruction showing the luggage contents.

Two images of the contents are produced: one from the nonresonant (6- and 7-MeV) gamma rays, which provides a 3-D image of the mass distribution within the inspection volume, and another of the nitrogen distribution using the resonant, 9.17-MeV gamma rays. A number of image-processing techniques are available (not automated at this stage of development) to ascertain the likelihood of the presence of explosives.

A more detailed description of each of these major subsystems is given below.

### 4. PROTON ACCELERATOR

The proton accelerator used for this project was an RFQ linac acquired by Los Alamos and modified and partially upgraded by the FAA for resonance absorption applications. One objective of the project is to evaluate the suitability for resonance transmission measurements of an RFQ linac (pulsed beam) in comparison with electrostatic accelerators (CW beam). The principal issue centers on the beam characteristics typical of an RFQ accelerator, e.g., the effect of beam emittance (energy and geometric) and the micro- and macro- structure of the pulsed beam on transmission measurements. Other considerations are inherent beam stability, size, cost, etc. These issues, as well as a detailed description of the accelerator and associated beam transport system, are discussed in detail in an accompanying paper [2092-60].

### 5. PROTON TARGET

The most prominent design issue with respect to the proton target is its ability to withstand the heat load imposed by the high-current proton beam. The original design requirement was for a 15-mA beam. This was subsequently relaxed to a 0.5-1.0 mA beam, although the targets used in these tests incorporated some of the features for the higher power levels. Other design considerations include minimization of unwanted secondary gamma-ray production in the copper backing and ease of fabrication.

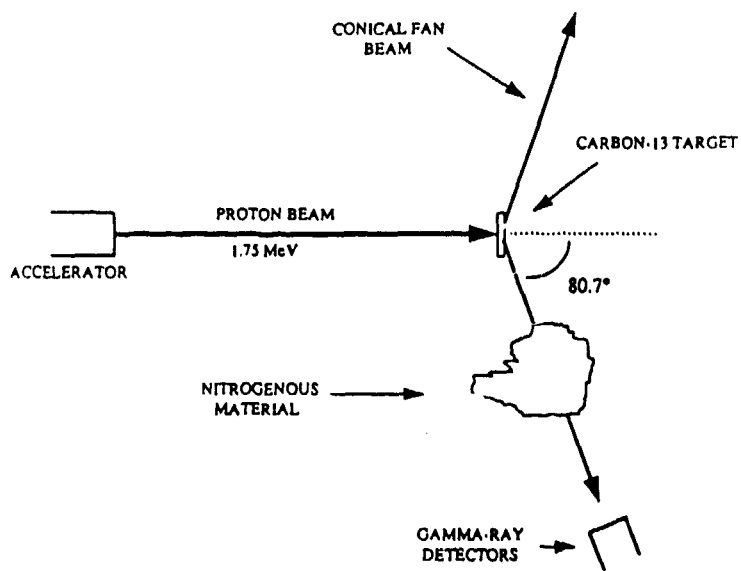


Figure 2. Resonance-absorption-based detection concept.

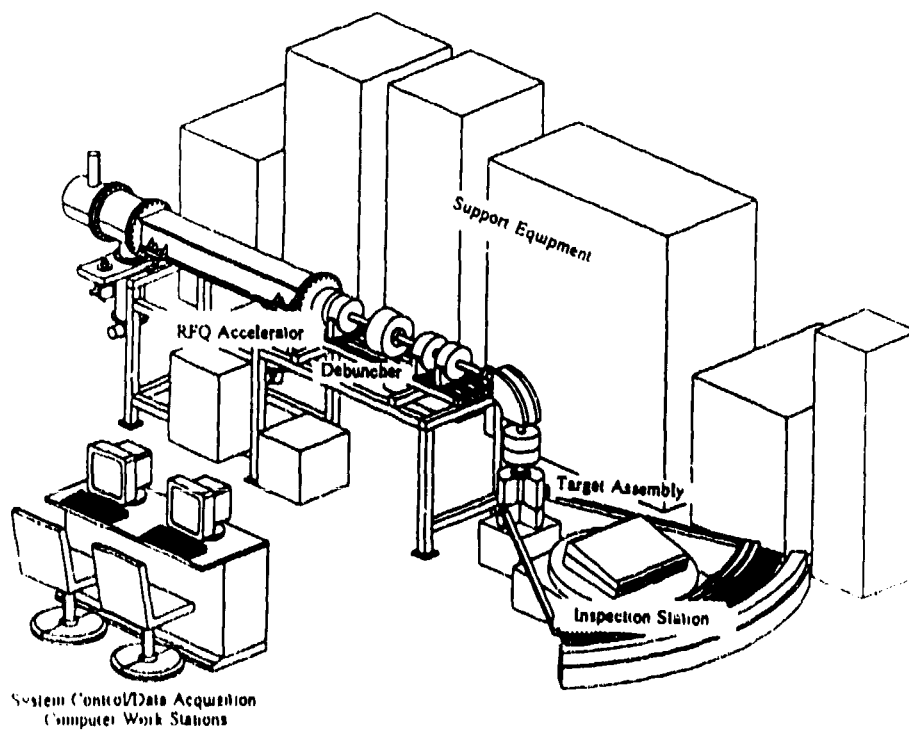


Figure 3. Physical configuration of the detection system.

Table I.  
Thick target coatings.

Target Set	Layer	Material	Thickness
#1	1	Carbon 13	148 $\mu\text{g}/\text{cm}^2$
	2	Hafnium	300 Å
	3	Gold	5750 Å
	4	Hafnium	300 Å
	5	Barium Fluoride	1300 Å
	6	Hafnium	300 Å
#2	1	Carbon 13	160 $\mu\text{g}/\text{cm}^2$
	2	Hafnium	500 Å
	3	Barium Fluoride	1300 Å
	4	Hafnium	300 Å
#3	1	Carbon 13	176 $\mu\text{g}/\text{cm}^2$
	2	Hafnium	300 Å
	3	Gold	5750 Å
	4	Hafnium	300 Å
	5	Barium Fluoride	1300 Å
	6	Tantalum	10 $\mu\text{m}$

The first generation designs were for power densities of  $\leq 4 \text{ kW}/\text{cm}^2$ . A water-cooled copper backing was used to dissipate the heat. The water is transported through channels machined into the back of the target to within 1.6 mm of its front face. The channel is in the form of a logarithmic spiral (see Fig 4), which produces a turbulent radial flow away from the central hot spot. Several coating variants were fabricated (see Table I) and tested. Excitation curves and gamma-ray spectra were obtained for a sample from each batch as a check on the thickness of deposited materials.

The Set # 1 duplicates our earliest design first tested in 1991 at power levels of  $\leq 1 \text{ kW}/\text{cm}^2$  at the University of Birmingham (UK) Dynamitron CW accelerator. In the others, the  $^{13}\text{C}$  thickness was increased to accommodate the inherent proton energy spread (estimated to be  $\geq 20 \text{ keV}$ ) associated with the accelerating process (bunching) of an RFQ accelerator. The purpose of the hafnium is to facilitate interlayer bonding; a layer of gold is necessary to degrade the proton energy to that of the fluorine resonance level; and, in #6, the tantalum is to further degrade the

proton energy to  $\leq 500 \text{ keV}$ , so that the gamma-ray background induced by the copper would be markedly lower. The coatings were applied by vapor deposition with a four-hearth electron-beam source. A quartz crystal monitor was employed to control coating thicknesses. The final thicknesses and coating densities were determined from either profilometer measurements of witness plates or from microbalance differential weights.

No degradation of these targets was detected in the course of operational testing of the detection system; however, the heat loading was only moderate (generally less than 2 kW over a period of  $\leq 200 \text{ h}$ ).

## 6. LUGGAGE MANIPULATOR

The luggage manipulator (see Fig 5) sequentially positions vertically and orients rotationally the luggage in the resonant energy beam to obtain the different viewing directions required for tomographic image reconstruction. For each vertical position, the luggage manipulator table rotates the bag in uniform increments through  $360^\circ$ . Upon completion of a rotational viewing sequence, the platform is raised or lowered by an amount determined by the beam width. This viewing sequence is repeated until the entire bag thickness is scanned. In these tests, either 32 or 64 viewing directions were employed. The slightly diverging beam was approximately 1.8-cm wide at the center of rotation of the turntable.

The manipulator table is capable of rotating and elevating luggage having maximum lateral dimensions of 91 cm (36 in) and a maximum of 41 cm (16 in) high. It is driven by stepping motors with shaft encoders that indicate the position of the table. The platform is mounted on an elevator that is driven by a ball-screw/ball-nut on each corner of the platform. The four ball nuts are driven by a single stepping motor through drive belts. Ball bushings on guide shafts guide the elevator, which is mounted on a tilt wedge for precise alignment of the manipulator platform with the beam direction.

The motion of the manipulator is controlled digitally from the data-acquisition computer work station. The number of rotational views and the viewing slice thickness are selectable operator input parameters. The duration of each view is determined by the number of recorded gamma-ray counts; each view is continued until the desired number of counts is obtained. The desired counting statistics also is an operator input parameter.

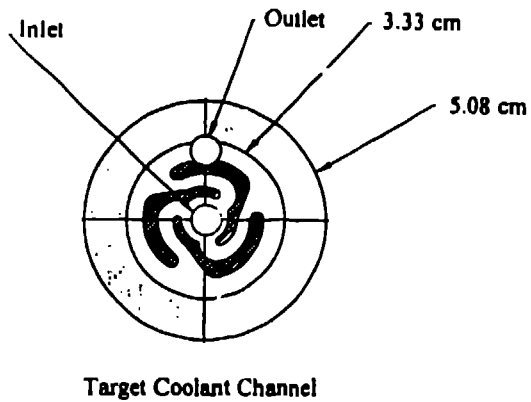


Figure 4. High-power target design.

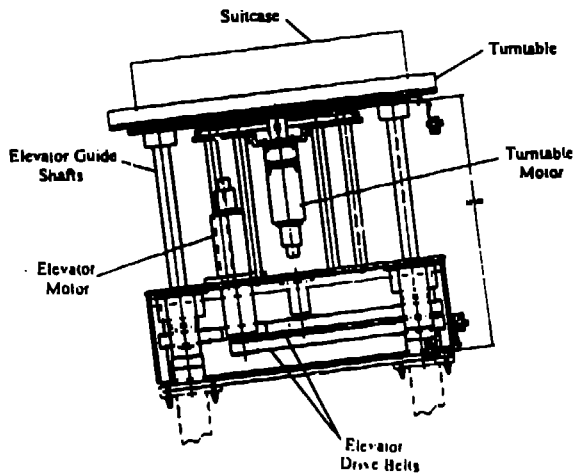


Figure 5. Luggage Manipulator.

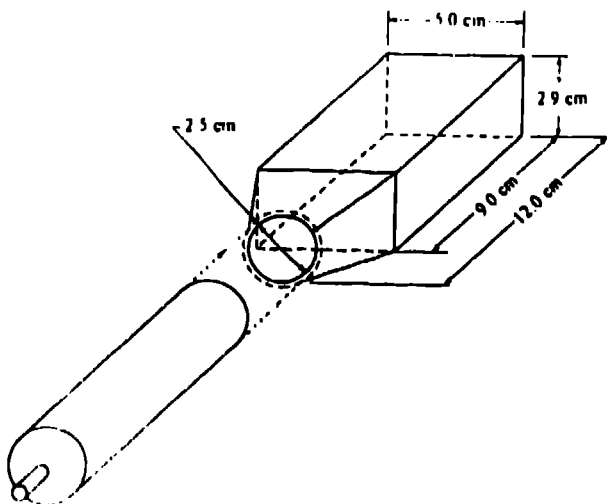


Figure 6. Tapered BGO crystal and light pipe.

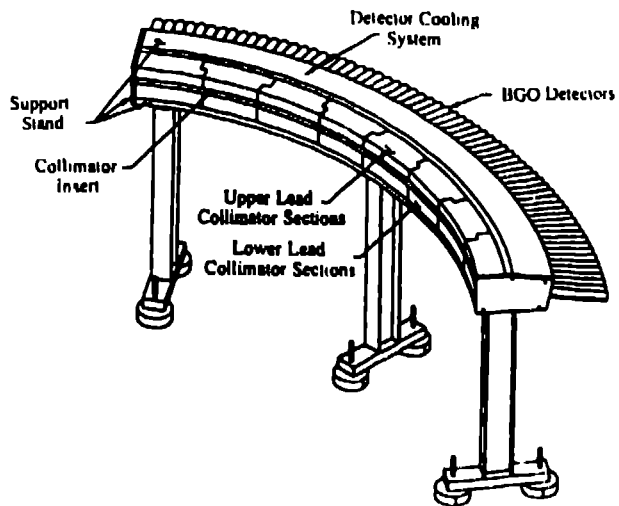


Figure 7. Collimated detector array.

## 7. GAMMA RAY DETECTOR SYSTEM

Selecting the optimum dimensions for individual gamma ray detectors is a difficult trade off between opposing factors: maximum spatial resolution requires small detectors, while maximum efficiency dictates larger detector crystals. Another consideration in the design process is the nature of the scintillator material, which affects efficiency, spectral resolution, and stability. Finally, the optical coupling of the scintillator crystal to the photomultiplier tube (PMT) can also materially affect performance. The design process for determining the best combination of detector parameters was iterative, involving extensive computer modeling of detector response and experimental tests of different scintillator materials, geometries, and PMT coupling approaches.

Bismuth germanate was chosen as the baseline scintillator material on the basis of its high stopping power (high Z), adequate spectral resolution (sufficient to resolve the 6- and 7- MeV resonance lines and the 9.17-MeV  $^{14}\text{N}$  resonance), and stability (but requiring auxiliary temperature stabilization). A detector diameter of 3 cm was chosen, which is the minimum size for an acceptable detector efficiency. The detector slit width is  $\approx 2$  cm, as dictated by the angular width of the resonance photon beam. The resultant average pixel size is  $\approx 2.0$  cm  $\times$  1.3 cm. The 3-D spatial resolution of the viewing system is a function of these dimensions and the number of tomographic viewing directions.

Several approaches for PMT optical coupling were investigated, but the most acceptable required tapering the crystal to match the aperture of the PMT. The resultant crystal geometry is shown in Fig 6. The custom-designed detectors were supplied by the Bicon Corporation. Sixty-four detector assemblies were required in order to span the lateral dimension of the specified inspection volume. The measured energy resolution of the detectors averaged  $\approx 15\%$ .

The detector mounts, beam collimator, and support stand were designed as an integral structure to support and align the BGO detectors and provide a 10-cm thick lead collimator slit. Figure 7 illustrates the assembled support system. Vitreous carbon spacers maintain the collimator slit spacing. Chilled-water lines were attached to the upper aluminum cover plate of the detector mounts to stabilize the scintillator crystal temperature at 17°C.

## 8. DATA ACQUISITION SYSTEM

The data acquisition system receives the signal output of the 64 detectors; processes and categorizes the data according to detector location, inspection slice, and viewing direction; and stores the data for transfer to the tomographic image processing system. It also provides the necessary hardware and software to control and monitor the luggage-inspection platform-motion equipment, accelerator, and high-voltage supplies. The general design guidelines were: 1) provide near-real-time output (i.e., a process rate of  $\approx 1.6 \cdot 10^6$  events/s), 2) minimum dead time contribution, and 3) use commercial hardware and software when possible.

The selected system is VMEbus-based, with VxWorks (Wind River Systems) as the real-time operating system. The VMEbus protocol permits 21 or more CPUs per crate. All software development was done on a Sun SPARC II work station, which permits convenient downloading of software to each CPU as executable code.

The detector signals feed the VMEMCA board (Fig. 8), which comprises two sections: 1) a commercial, 3U-sized, 68030 CPU with dual-ported memory, PROMS, serial I/O, etc.; and a daughter-board interface that allows custom boards to be attached; and 2) a custom designed analog processing section with twelve independent channels, each containing a low-level discriminator (LLD), programmable gain amplifier (PGA), charge integrator, analog-to-digital converter(ADC); and a first-in first-out memory (FIFO).

When an input pulse from the gamma-ray detector exceeds the LLD threshold, the charge integrator constructs a delayed version of the pulse. The integration time is software-selectable from 100 ns to 12 ms (a minimum of 400 ns is used, in keeping with the bismuth germanate decay time of 300 ns). After charge integration, the signal is digitized by the ADC and stored in the FIFO. The dead time contribution, not including integration time is  $< 100$ ns. The program executed by VMEMCA's CPU sequentially reads each FIFO of the analog section, which is tagged with the detector ID and the luggage platform vertical and rotational position, and provides the memory address used in constructing an energy histogram and an ROI. For a 125-kHz single-channel instantaneous rate, the dead time ranges from 6% to 16%. Tests show the system will adequately resolve our multi-energy spectra for all anticipated operating conditions.



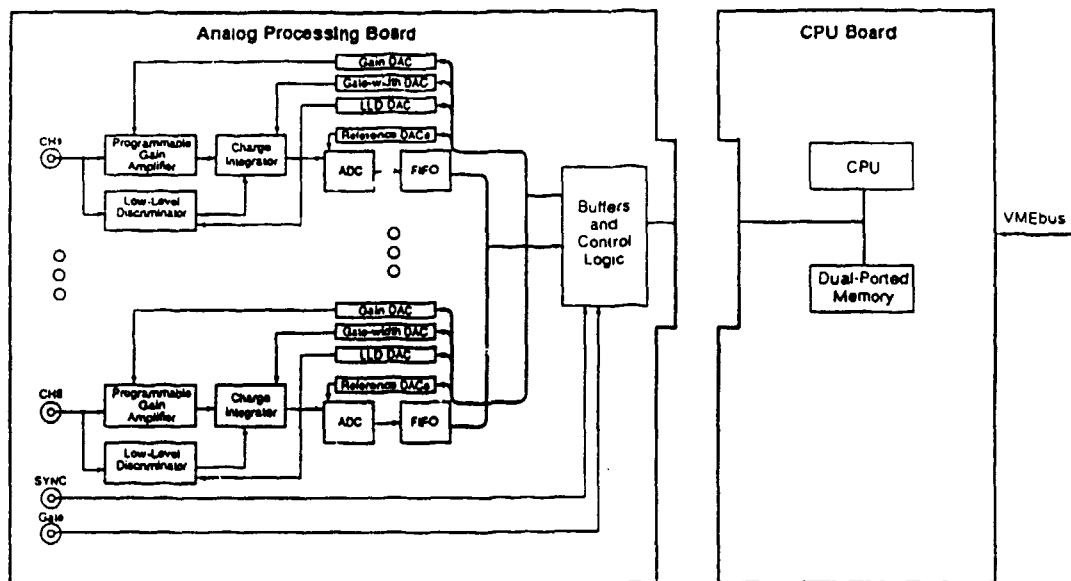


Figure 8. VMEMCA block diagram

## 9. TOMOGRAPHIC IMAGE PROCESSING

A tomographic approach was chosen for analyzing the resonance transmission measurements because, in principle, it can provide a detailed 3-D mapping of the nitrogen density distribution within the luggage. This generally is necessary for analyzing irregularly shaped explosives devices. As noted above, transmission measurements are also made at off-resonance energies, from which the mass distribution within the luggage can be obtained as well. Although the nitrogen density alone can be a reliable signature, the combination of nitrogen density and total density clearly improves the accuracy of material identification, especially for cases involving marginal counting statistics.

The image processing is built around KHOROS, a fully developed, public domain code (University of New Mexico) for information processing, data visualization, and software development. KHOROS also allows the inclusion of special purpose routines developed by the user. A number of these have been written for this project, although some are not yet used at this early stage of testing. The tomographic reconstruction software is incorporated into KHOROS as a special-purpose routine. Details of the specially developed reconstruction algorithms and some of the details of KHOROS are presented in an accompanying paper [2092-58].

At the current stage of development, the tomographic algorithm reconstructs a cross sectional 2-D image of each slice. These are convenient for visual (non automated) interpretation of the images. The cross sectional images can be displayed sequentially and, from interslice comparisons, the vertical locations of objects can be established. Although an initial version of a 3-D image reconstruction algorithm has been completed and partially tested, it has not been integrated into the system.

As indicated earlier, images are reconstructed of both the total density distribution and of the nitrogen density distribution ("nitrograms"). The shape of higher density objects generally can be determined from the nonresonance image. Any objects with density outside the expected range for explosives ( $\approx 1.0 - 1.9 \text{ g/cm}^3$ ) are inferred to be a non explosive. Objects with densities within the above range are compared to the nitrogram image and if the nitrogram indicates a significant nitrogen density at the corresponding location, the object is presumed to be an explosive. Automation of the preceding simple alarm protocol and others under consideration is not anticipated until an extensive image data base is available for evaluation and optimization of the system.

## 10. INITIAL DETECTION EXPERIMENTS

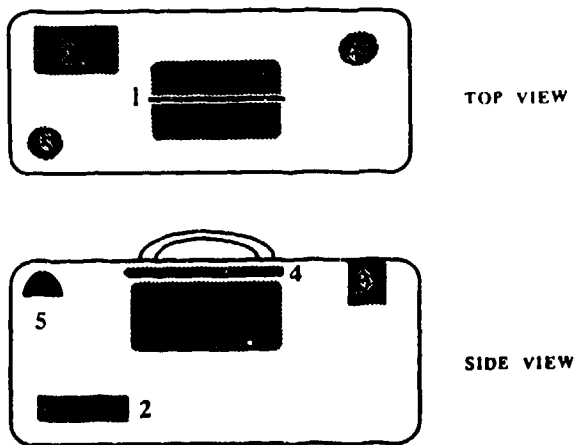
Because of programmatic time constraints, detectability testing of the EDS system using live explosives was started immediately upon completion of system assembly. Thus, the tests reported below are a part of the preliminary system optimization experiments and do not represent the expected capabilities of the system. Nevertheless, they provide an indication of the system's performance potential.

A blind-test system-detectability demonstration was conducted by an FAA-led explosive handling team. The team, in collaboration with explosives development organizations at Los Alamos, independently acquired a range of explosive types, densities, masses, nitrogen content, and shapes for these tests. Selected explosives were placed in FAA-supplied (unclaimed) luggage at a remote magazine, and delivered by this team to the experimental site. The individual bags were placed on the inspection table for each test, monitored during the luggage inspection period, and then returned to a holding area. Knowledge of the luggage contents was restricted to the FAA team. The blind-test protocol provides for an extended period of time following this test series before the experimental team must declare the detection results. This period is to permit some of the software debugging, system calibration, etc., that normally would have taken place prior to the demonstration. After the detection results are declared, the FAA team will reveal the actual contents of the luggage to the experimental team. A total of fourteen bags were inspected in these blind tests (the majority with explosives but some with explosives simulants), but the declared results of these are not yet available. However, a system calibration test can be reported, which was done in the same manner as the other tests, but with a piece of luggage containing known explosives and simulants. Although a very limited test, it provides an indication of the minimum potential capabilities of the technique.

Figure 9 shows a sketch of the calibration bag, its explosives contents, and the operational test parameters. The system calibration bag was prepared by the FAA team and contains specimens representing four explosive types (see Table II) and geometries that range in total mass from 2/3 to 1 1/2 of the particular explosives threat quantity employed in this project. (The threat quantity represents the minimum amount of explosive for which the system was designed to detect.)

The explosive sheets are representative of the geometric extremes for practical explosive devices and, for this calibration test, were oriented approximately perpendicular and parallel to the viewing direction.

As noted before, the image processing system constructs a tomographic image of the cross section of the bag for each viewing slice. Image reconstructions of two of the slices near the top of the bag are shown in Fig 10 that illustrate the detection capabilities and limitations of the unoptimized system in these first tests. The image pairs are from the non-resonance (left) and resonance (right) transmission measurements. The viewing perspective is from



Test D-3, Bag # 3  
(Calibration Bag)

INSPECTION PARAMETERS		TEST EXPLOSIVES	
VIEWS	64	1	DETA SHEET, 1 mm thick 1.09 g threat
SLICE THICKNESS	1.2 cm	2	BARATOL, 2 in Cyl 1.18 g threat
COUNTS/VIEW	400	3	9205 PBX, 2 in Cyl 1.48 g threat
SLICES	6	4	DETA SHEET (C4), 5 mm 1.07 g threat
BAG CONTENTS	Counties	5	9404 PBX SIM. Item 0.65 g threat

Table II  
Test Explosives Physical Properties  
(nominal values)

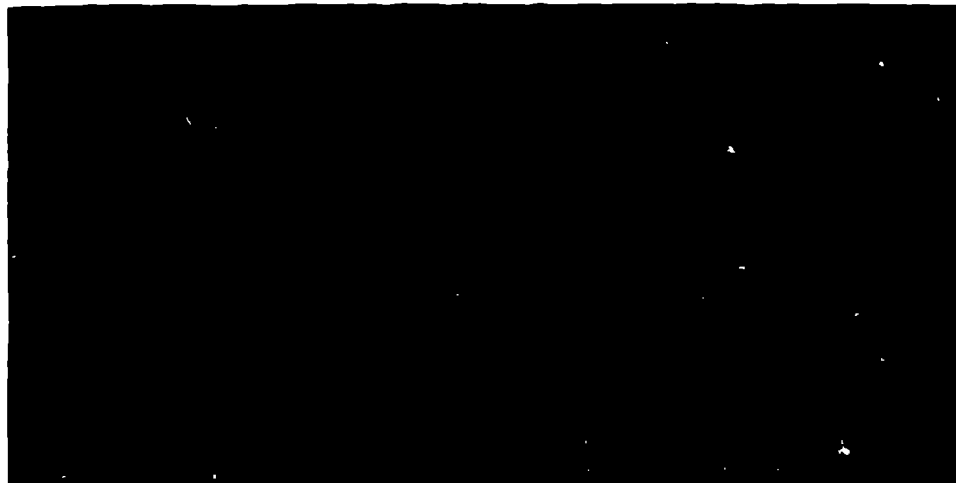
Name	Principal Constituents	Density g/cm <sup>3</sup>	<sup>14</sup> N Density g/cm <sup>3</sup>
Deta Sheet	75% PETN	1.5	0.19
Baratol	TNT/Bar(NO <sub>3</sub> ) <sub>2</sub>	2.5	0.37
9205 PBX	92% RDX	1.7	0.59
Deta Sheet	63% PETN	1.5	0.17
9404 PBX	94% HMX	1.8	0.64

Figure 9. Calibration-bag test parameters.

Slice 2



Slice 4



Non Resonance Image

Resonance Image (Nitrogram)

**Figure 10. Image reconstructions of the calibration bag.**

above the bag, looking downward (i.e., the top view in Fig. 9) and shows the density distribution over two selected horizontal cross sections (slices) of the bag. In these reconstruction displays, the longitudinal axis of the bag is rotated clockwise approximately 45° from the top of the page.

Slice 2 is approximately 3 cm below the top of the bag, and at this level intersects test objects 3, 4, and 5 (see Fig. 9, side view). The upper, high density object (bright area) in the reconstructions is the 9205 PBX (seen in both slices) and the lower object is a hemispherically shaped 9404 PBX simulant (#5 in Fig. 9). The horizontal sheet explosive (#4) was not precisely parallel to the plane of plane of the beam, and slice 2 intersects only about 1/3 of the sheet. In the left hand reconstruction of slice 2, the diffuse, brighter region between and slightly to the right of test objects 3 and 5 is the portion of the sheet explosive (#4) noted above. The nitrogram of slice 2 clearly indicates the presence of high-density nitrogen in 3 and 5, but not for the sheet explosive (#4). However visual comparisons of successive slices in the original images marginally suggest the presence of nitrogen.

In slice 4 (approximately 5 cm below the top of the bag), the beam still intersects test objects 3 and 5, but now the vertical sheet (#1) has come into view. In the lower right quadrant of the reconstruction, a calibration standard positioned just outside the bag also has come into view. The vertical sheet (aligned with the longitudinal axis of the bag) can also be seen near the center of the non resonance reconstruction. However, there is no indication of nitrogen associated with the sheet explosive. This result is not surprising, since the fundamental detectability limit of the system is directly related to the effective voxel size of the viewing system, and explosive samples with a dimension comparable to the minimum voxel dimension, as is the case for the sheet explosives, generally will appear as a lower density object (both total density and nitrogen density).

A 3-D tomographic approach was included in the system design concept, in part, to determine whether it would significantly improve detectability in the case of sheet explosives. However, 3-D imagery, and the associated special image processing techniques, is yet to be applied. Another known deficiency in the tested detection system is associated with the unoptimized beam transport system, which, because of an improperly focused proton beam, caused a reduction in the effective nitrogen cross section, which would also contribute to a lower apparent nitrogen density.

## 11. CONCLUSIONS

We conclude from this very limited test that a detection system based on this approach should readily detect nitrogen explosives in amounts well below our design objective, especially if they are in a compact geometry. We expect significant improvements from various system optimization measures and from the use of 3-D reconstructions. As these initial results suggest, these improvements will be necessary for detecting low-nitrogen-content explosives and sheet explosives. However, the actual detectability limits of this approach as well as the very important issue of false alarms cannot be addressed until system optimization is complete and an appropriate statistical data base acquired.

## 12. REFERENCES

1. The Feasibility of Detecting FAA-Threat Quantities of Explosives in Luggage and Cargo Using Nuclear Resonance Absorption in Nitrogen, Phase I Final Report, October 1989, Los Alamos National Laboratory, Advanced Nuclear Technology, Internal Report.
2. Goldberg, M. B., Vartsky, D., et. al., Informal Proposal, Soreq Nuclear Research Center, Yavne, Israel, December 1985.
3. Hannah, S.S. and Meyer-Schutzmeister, Luise, "Resonant Absorption by the 9.17-MeV Level in  $^{14}\text{N}$ ", Physical Review 115, 4, (1959).
4. Biesiot, W. and Smith, Ph. B., "Parameters of the 9.17-MeV Level in  $^{14}\text{N}$ ", Physical Review C 24, 6, (1981).
5. Vartsky, D., Goldberg, M. B., Engler, G., Goldschmidt, A., Breskin, A., Morgado, R. E., Hollas, C. L., Ussery, L. E., Berman, B. L., and Moss, C. E., "The Total Width of the 9.17-MeV Level in  $^{14}\text{N}$ ", Nuclear Physics A505 (1989) 328-336.
6. Seagrave, J. D., "Radiative Capture of Protons by  $^{13}\text{C}$ ", Physical Review 85, 2, (1952)